



## Particle Diagnostics Using Mie Scattering and Image Intensification Techniques

R. L. McGuire, J. W. L. Lewis,  
D. P. Weaver, and B. P. Curry  
ARO, Inc.

January 1980

Final Report for Period August — October 1978

Approved for public release; distribution unlimited.

Property of U. S. Air Force  
AEDC LIBRARY  
F4089-77 C-2003

**ARNOLD ENGINEERING DEVELOPMENT CENTER  
ARNOLD AIR FORCE STATION, TENNESSEE  
AIR FORCE SYSTEMS COMMAND  
UNITED STATES AIR FORCE**

## NOTICES

When U. S. Government drawings, specifications, or other data are used for any purpose other than a definitely related Government procurement operation, the Government thereby incurs no responsibility nor any obligation whatsoever, and the fact that the Government may have formulated, furnished, or in any way supplied the said drawings, specifications, or other data, is not to be regarded by implication or otherwise, or in any manner licensing the holder or any other person or corporation, or conveying any rights or permission to manufacture, use, or sell any patented invention that may in any way be related thereto.

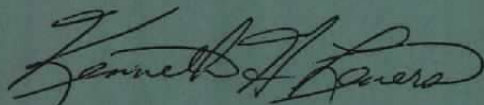
Qualified users may obtain copies of this report from the Defense Technical Information Center.

References to named commercial products in this report are not to be considered in any sense as an indorsement of the product by the United States Air Force or the Government.

This report has been reviewed by the Office of Public Affairs (PA) and is releasable to the National Technical Information Service (NTIS). At NTIS, it will be available to the general public, including foreign nations.

## APPROVAL STATEMENT

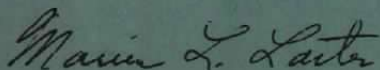
This report has been reviewed and approved.



KENNETH H. LENERS, Captain, USAF  
Project Manager  
Directorate of Technology

Approved for publication:

FOR THE COMMANDER



MARION L. LASTER  
Director of Technology  
Deputy for Operations

# UNCLASSIFIED

REPORT DOCUMENTATION PAGE		READ INSTRUCTIONS BEFORE COMPLETING FORM
1 REPORT NUMBER AEDC-TR-79-42	2 GOVT ACCESSION NO.	3 RECIPIENT'S CATALOG NUMBER
4 TITLE (and Subtitle) PARTICLE DIAGNOSTICS USING MIE SCATTERING AND IMAGE INTENSIFICATION TECHNIQUES		5 TYPE OF REPORT & PERIOD COVERED Final Report, August - October 1978
		6 PERFORMING ORG REPORT NUMBER
7 AUTHOR(s) R. L. McGuire, J. W. L. Lewis, D. P. Weaver, and B. P. Curry, ARO, Inc., A Sverdrup Corporation Company		8 CONTRACT OR GRANT NUMBER(s)
9 PERFORMING ORGANIZATION NAME AND ADDRESS Arnold Engineering Development Center Air Force Systems Command Arnold Air Force Station, Tennessee 37389		10 PROGRAM ELEMENT PROJECT, TASK AREA & WORK UNIT NUMBERS Program Element 65807F
11 CONTROLLING OFFICE NAME AND ADDRESS Arnold Engineering Development Center/DOS Air Force Systems Command Arnold Air Force Station, Tennessee 37389		12 REPORT DATE January 1980
		13 NUMBER OF PAGES 37
14 MONITORING AGENCY NAME & ADDRESS (if different from Controlling Office)		15 SECURITY CLASS (of this report)  UNCLASSIFIED
		15a DECLASSIFICATION DOWNGRADING SCHEDULE N/A
16 DISTRIBUTION STATEMENT (of this Report)  Approved for public release; distribution unlimited		
17 DISTRIBUTION STATEMENT (of the abstract entered in Block 20, if different from Report)		
18 SUPPLEMENTARY NOTES  Available in Defense Technical Information Center (DTIC).		
19 KEY WORDS (Continue on reverse side if necessary and identify by block number) flow visualization Mie scattering		
20 ABSTRACT (Continue on reverse side if necessary and identify by block number) The visualization of a particulate-laden flow field immersed within a hypersonic flow has been achieved using Mie scattering. The visualization technique employed the injection of a modulated laser beam which was expanded to provide observation of a broad spatial region of the particulate plume. The Mie scattered radiation was detected by an image intensifier tube, the output of which was detected by a fast-framing camera. A description is provided of this system, the analysis of the data, and the results.		

# UNCLASSIFIED

## **PREFACE**

The work reported herein was conducted by the Arnold Engineering Development Center (AEDC), Air Force Systems Command (AFSC). The results of the research were obtained by ARO, Inc., AEDC Division (a Sverdrup Corporation Company), operating contractor for the AEDC, AFSC, Arnold Air Force Station, Tennessee, under ARO Project Number V32I-P2A. The Air Force project manager was Captain Stanislaus L. Ludwig (CF), AEDC/DOT. The data analysis was completed on August 18, 1978, and the manuscript was submitted for publication on March 30, 1979.

## CONTENTS

	<u>Page</u>
1.0 INTRODUCTION .....	5
2.0 APPLICATION CONFIGURATION AND THEORY	
2.1 Configuration of Application .....	6
2.2 Mie Scattering Theory for Localized Particles .....	6
2.3 Mie Scattering from Extended Regions .....	8
3.0 EXPERIMENTAL APPARATUS .....	12
4.0 RESULTS	
4.1 Visualization Results .....	15
4.2 Transmission Results .....	16
5.0 CONCLUSIONS AND RECOMMENDATIONS .....	17
REFERENCES .....	18

## ILLUSTRATIONS

### Figure

1. Particle-Laden Flow-Field Configuration .....	19
2. Scattering Geometry for Single Particle with Light Incident along $\hat{Z}$ Axis and Polarization Vector along $\hat{X}$ Axis .....	20
3. Experimental Configuration: Flow Visualization and Transmission Measurements .....	21
4. Visualization Geometry .....	22
5. Typical Intensifier Response Curve .....	23
6. Transmission Channel Configuration .....	24
7. Flow Visualization of Tungsten Particulate Flow, Run 5,986, Visualization Signal Resulting from Mie Scattered Radiation Combined with Near-Infrared Particulate Luminosity .....	25
8. Flow Visualization of Tungsten Particulate Flow, Run 5,986, Visualization Signal Source Consisting Entirely of Near-Infrared Particulate Luminosity .....	27
9. Flow Visualization of Tungsten Carbide Particulate Flow, Run 5,990, Visualization Signal Source Consisting Entirely of Mie Scattered Radiation .....	28

10. Flow Visualization of Silicon Carbide Particulate Flow, Run 5,991, Visualization Signal Source Resulting from Mie Scattered Radiation Combined with Near-Infrared Particulate Luminosity .....	29
11. Flow Visualization of Tungsten Carbide Particulate Flow, Run 5,996 at 111 msec from Tunnel Arc Voltage, Visualization Signal Source Consisting of Very Weak Near-Infrared Particle Luminosity and Mie Scattered Radiation .....	30
12. Flow Visualization of Tungsten Carbide Particulate Flow, Run 5,996 at 131 msec from Arc Voltage, Visualization Signal Source Consisting of Strong Near-Infrared Particulate Luminosity and Mie Scattered Radiation .....	31
13. Flow Visualization of Tungsten Particulate Flow, Run 5,997, with a Particle Plume Temperature of Approximately 1,578 K, Visualization Signal Source Consisting of Near-Infrared Particulate Luminosity and Mie Scattered Radiation .....	32

## TABLES

1. Flux Integral IF .....	33
2. Exemplary Data Photograph Summary .....	33
3. Mass Flow Rate -Exemplary Data Summary .....	33
4. Exemplary Transmission Data .....	34

NOMENCLATURE .....	35
--------------------	----

## 1.0 INTRODUCTION

There is a continuing need for measurement capabilities of particulates encountered in ground-based simulation facilities. These particles may be generated by the source of the simulation flow field or, in some cases, by the object, such as a rocket engine, which is being tested. The characterization provided by the diagnostics can be quite varied, ranging from mere determination of the existence of the particulates to the more complete specification of particle size distribution function and identification of particulate species and the three-dimensional velocity distribution function. For ground-based simulation facilities as diverse as those of the Arnold Engineering Development Center (AEDC), the range of particle sizes and densities, particulate species, flow velocities, required time and space resolution, and spatial extent of the particulates obviously provides multidimensional diagnostics requirements. Therefore, it should not be surprising that no one measurement approach is adequate for the spectrum of testing requirements. Simple examples of the restriction of application regimes of various techniques are a) the limitation of current holographic capability by particles of super-micron sizes; and b) the limitation to low particulate densities of techniques which require the presence of no more than one to two particles within the focal volume of an injected, focused laser beam. It cannot be too strongly emphasized that the regimes of application of many techniques become oppressively constraining when the desire for short time resolution in pulsed flow facilities is introduced. Perspective of pulsed flow field-particulate diagnostics requirements is afforded by noting that a flow-field duration of 100 msec and a desired time resolution on the order of 1 msec are not uncommon test parameters either for ground-based test facilities or for pulsed liquid rocket engine plume exhausts. If one includes certain solid rocket engines in this consideration, the requirements increase in stringency by an order of magnitude (i.e., to 10-msec duration and 100- $\mu$ sec resolution). Clearly, nonroutine diagnostic techniques are required.

Presented in this work is the description of a particulate visualization technique which was employed recently for characterization of a nominal 100-msec-duration flow field and for which time resolution on the order of 1 msec was achieved. As will be presented in detail, the application of interest was the visualization of the spatial extent of particulates injected into a coflowing hypersonic flow field which was provided by the AEDC von Kármán Gas Dynamics Facility (VKF) arc-heated Hypervelocity Wind Tunnel (F). The spatial extent of the injected particulates was relatively large, and qualitative knowledge of the density distribution was desired. Information on the magnitude of heating and the subsequent radiation of the injected particles following traversal of a shock system was also desired.

The approach taken to satisfy these test requirements was the injection into the flow field of a laser beam which was expanded into a wide plane sheet configuration. The interaction

of this beam with the particulates produced Mie scattered radiation by which the scene was viewed and which was detected with an image intensifier. To achieve the desired time resolution required that the output of the intensifier be viewed with a rapid-framing camera. Modulation of the laser beam at the 100-percent level provided images produced by the particulate emission alone, and these data yielded information regarding particulate heating. Data reduction and analysis were achieved using computer analysis of the fast-scan photographs. A more complete description of the system, the application of interest, and the results is presented in the following section. Finally, an order-of-magnitude comparison of the sensitivity of the image intensifier detection system to the sensitivity of the more conventional photographic method is provided.

## **2.0 APPLICATION CONFIGURATION AND THEORY**

### **2.1 CONFIGURATION OF APPLICATION**

The particulate-laden flow field which is to be considered is partially sketched in Fig. 1, which shows the source from which the particles are injected into a coflowing hypersonic flowfield. (The gas dynamic shock systems are not shown in Fig. 1.) The laser beam is expanded to illuminate a substantial axial length of the particle plume exhaust. The Mie scattered radiation is collected and detected by the image intensifier optical system.

Prior to the application of this system to the visualization task, as shown in Fig. 1, a feasibility calculation was performed with the goal of determining the photon rate of irradiation of a picture element, or pixel, of the image intensifier tube. The results of this calculation can be compared with the calculated performance of a system which employs photographic film detection rather than intensification followed by photography. The calculation presented in the following sections proceeds thus: a) description of single-particle Mie scattering; b) generalization of the single-particle theory to the situation as shown in Fig. 1; and c) calculation of the response of a photographic system.

### **2.2 MIE SCATTERING THEORY FOR LOCALIZED PARTICLES**

The incoherent scattering of an incident plane wave by a single dielectric sphere is described exactly by the Mie scattering theory, which was developed in the first decade of the 20th century through the collective efforts of Lorentz, Mie, Debye, and others. A comprehensive derivation of Mie scattering theory is given in Ref. 1. Practical application of Mie scattering to problems of current interest has been made possible comparatively recently by the employment of modern digital computing techniques, which are exemplified by Ref. 2. For the purposes of the calculations presented in this report the authors use a computer



program described in Ref. 3 and refer the reader to the literature cited therein for details of the calculation methodology.

Reference to Fig. 2 will aid the reader in understanding the general attributes of Mie scattering from a single particle. A plane wave of wavelength  $\lambda$  and an electric field polarized along the  $\hat{x}$  axis are incident on a particle of complex refractive index  $\eta = \eta_r - i\kappa$ , which is located at the origin. The direction of propagation of the incident wave is along the positive  $\hat{z}$  axis; i.e., the particle is illuminated from below. Upon interaction with the particle the light is scattered, and if  $\kappa \neq 0$ , a portion of its energy is lost to absorption by the particle. For an observer whose coordinates are  $(r, \theta, \phi)$ , the intensity of the light scattered without change in wavelength is given by

$$I(r, \theta, \phi, \eta, \kappa) = \frac{I_0}{(kr)^2} \left[ i_1(x, \theta, \eta) \sin^2 \phi + i_2(x, \theta, \eta) \cos^2 \phi \right] \quad (1)$$

where

$I_0$  is the incident light intensity (energy flux per unit time per unit area),

$k = 2\pi/\lambda$  is the wave number of incident light,

$r$  is the distance from the particle to the observer,

$x = \pi D/\lambda$  is the particle size parameter based on diameter  $D$ ,

$\phi$  is the azimuth of the scattering plane, and

$\theta$  is the polar scattering angle.

The computer-generated Mie intensity functions  $i_1(x, \theta, \eta)$  and  $i_2(x, \theta, \eta)$  correspond, respectively, to light scattered with its electric field oriented perpendicular and parallel to the scattering plane (the  $\vec{r}, \hat{z}$  plane).

In applications of Mie scattering one usually must consider scattering by a large number of particles (within a specified, finite volume) which may have a multiplicity of sizes (polydispersion) and which are viewed by a detector whose optics subtend a finite solid angle. In such cases, Eq. (1) must be replaced by

$$\Phi(r, \theta_s, \phi_s, \eta, \ell_s) = \int_0^{\ell_s} \int_0^{\infty} \int_{\phi_s - \frac{\Delta\phi_s}{2}}^{\phi_s + \frac{\Delta\phi_s}{2}} \int_{\theta_s - \frac{\Delta\theta_s}{2}}^{\theta_s + \frac{\Delta\theta_s}{2}} \frac{d\eta(\ell, x)}{dx} \left[ \frac{d\sigma_1}{d\Omega}(x, \theta, \phi, \eta) + \frac{d\sigma_2}{d\Omega}(x, \theta, \phi, \eta) \right] \sin \theta d\theta d\phi dx d\ell \quad (2)$$

where  $\Phi_0$  is the incident power of the illuminating beam;  $dn(\ell, x)/dx$  is the number density per unit size interval of particles whose size parameter is  $x$  and which are located at position  $\ell$ ; and  $\ell_s$  is the projection of the scattering volume along the optical axis. The differential scattering cross sections for the two orthogonal polarization states of the scattered light are related to the Mie functions by

$$\frac{d\sigma_1}{d\Omega}(x, \theta, \phi, \eta) = \frac{i_1}{k^2}(x, \theta, \eta) \sin^2 \phi$$

and (3)

$$\frac{d\sigma_2}{d\Omega}(x, \theta, \phi, \eta) = \frac{i_2}{k^2}(x, \theta, \eta) \cos^2 \phi$$

The subtended angles appearing in the limits of the angular integrals in Eq. (2) are obtained from the standard geometrical optics equations.

### 2.3 MIE SCATTERING FROM EXTENDED REGIONS

Once the scattering equations for localized particles (including polydisperse samples) have been obtained, the next task in the feasibility calculation is to include effects caused by the extension of the source, as shown in Fig. 1, for the application at hand. The axial region of interest was approximately 30 cm (12 in.), extending downstream from the source exit plane. As shown in Fig. 1, a thin slab of the particulate flow field is irradiated by the laser beam. The  $\hat{x}$  axis is along the flow, and the intensifier is located in the  $\hat{y}, \hat{z}$  plane at a distance

$L$  from the flow centerline and an angle  $\alpha$  from the direction of the beam propagation. The particle plume is illuminated from below by a beam-expanded laser situated at  $-\hat{z}_L$  whose beam has been expanded to a divergence angle  $\beta_0 = \tan^{-1} \hat{x}_0/z_L$  where  $x_0$  is half the axial "look distance." For these calculations  $\hat{x}_0$  was assumed to be 15 cm ( $\cong$  6 in.) and the laser distance  $\hat{z}_L$  was taken to be 67.5 cm ( $\cong$  27 in.). Figure 1 shows scattering from a particle which is located at  $\hat{x}_p, \hat{y}_p, \hat{z}_p$ , with  $-d/2 \leq y_p \leq d/2$  (where  $d$  is the small dimension of the laser beam) and which is illuminated by an incident ray offset from the laser axis by angle  $\beta$ , with  $-\beta_0 \leq \beta \leq \beta_0$ . Note that the plane of polarization of the incident light is the  $\hat{x}, \hat{z}$  plane with respect to the particle shown, the scattering coordinates are  $r', \theta', \phi'$ , and the results must, of course, be integrated over all particle locations which can be seen by the intensifier.

The intensifier is composed of many small resolution elements (pixels), each of which subtends a different solid angle and looks at a different region of the flow. Because the subtended angle of each pixel is very small, we assume the light flux into each pixel is the same as that at the center of the intensifier. For simplicity we also ignore the spatial nonuniformities of the particle plume and of the expanded incident laser beam, assume spherical particles of known refractive index, and consider a single particle size, or a monodisperse distribution function. Consequences of departure from these and other idealizations will be discussed in a later section.

Invoking these simplifying assumptions, we write the total scattered flux received by each pixel of the intensifier as

$$\Phi = \Phi_0 \left( \frac{\pi}{\lambda^2} \right) \left( \frac{A_{\text{beam}} d}{A_{\text{pixel}}} \right) I \quad (4)$$

where

$$I = \frac{1}{d} \iiint \left[ i_1(x, \theta', \eta) \sin^2 \phi' + i_2(x, \theta', \eta) \cos^2 \phi' \right] dr' \sin \theta' d\theta' d\phi'$$

with the appropriate limits on  $r', \theta', \phi'$ ;  $A_0$  is the area of a pixel. The integration limits were obtained as follows:

- From Fig. 1 one sees that  $L \sin \alpha - (d/2) \leq r' \sin \theta' \sin \phi' \leq L \sin \alpha + (d/2)$ .
- Since the intensifier diameter is 2.3 cm (0.9 in.) and its assumed "look distance" is 30 cm, its demagnification factor is  $M = 2.3/30 = 0.077$ .

- c) On the assumption of a lens of focal length  $f = 6$  cm, the appropriate distance from the intensifier to the plume centerline required to fill the intensifier face was calculated with the relation

$$\frac{L}{f} = 1 + \frac{1}{M}$$

and  $L$  was found to equal 86 cm.

- d) Assuming symmetry about the  $\hat{y}$  axis, we obtain

$$\left( \frac{L}{x_o} \sin \alpha \cos \beta_o \right) \leq \tan \phi' \leq \left( \frac{L}{x_o} \sin \alpha \cos \beta_o \right)$$

and

$$\alpha \leq \theta \leq \tan^{-1} \left\{ \frac{\left[ \left( L \sin \alpha \right)^2 + \left( x_o \sec \beta_o \right)^2 \left( 1 + \frac{R_b}{Z_L} \right) \right]^{1/2}}{\left( L \cos \alpha + Z_L \right) \sec \beta_o - Z_L \sec \beta_L \sec \beta_o \left( 1 + \frac{R_b}{Z_L} \right)} \right\}$$

where  $R_b$ , the radius of the plume boundary at the intensifier axial station, was assumed to be 11.25 cm.

Using these relations we determined the following angular limits:

$$a) 75.4^\circ \leq \phi' \leq 104.6^\circ \text{ and } 45^\circ \leq \theta' \leq 51.2^\circ$$

for  $\alpha = 45$  deg

and

$$b) 79.7^\circ \leq \phi' \leq 100.3^\circ \text{ and } 90^\circ \leq \theta' \leq 97.5^\circ$$

for  $\alpha = 90$  deg

These values were used to calculate the integral  $I$  for a range of spherical particle diameters in the range of  $1 \mu\text{m}$ , which for  $\lambda = 514.5$  nm yields a size parameter  $x = 6.11$ . In addition, the index of refraction,  $\eta$ , was assumed to be 2.68 (Ref. 4). The results are shown in Table 1. Because of the integration of the Mie functions over a wide angular range, which means that many Mie resonances are included in the integral, no simple trend is observed in Table 1.

However, it is seen that an order-of-magnitude estimate is possible for each value of  $\alpha$  (e.g.,  $IF \cong 1$  to 10 for  $\alpha = 90$  deg).

Further, for the conditions of this experiment, the quantity

$$\left( \frac{A_o}{A_{beam}} \cdot \frac{d}{k^2} \right) = 2.5 \times 10^{-18} \text{ cm}^3$$

and a typical number density is assumed to be  $10^6 \text{ cm}^{-3}$ ; hence,

$$\Phi / \Phi = 2.5 \times (10^{-12} \text{ to } 10^{-11})$$

Finally, assuming the injected laser power to be on the order of one watt, it is found that, for these conditions, each intensifier pixel receives a flux of order  $10^7$  photons/sec.

To determine the detectability of such a photon rate per pixel, one must determine the equivalent photon rate for the dark current of the tube. Assuming the dark current density to be equivalent to an input photon flux density of  $5 \times 10^4 \text{ photons/sec/cm}^2$ \* and taking the resolution element to be 0.07 mm, one finds the photon noise rate of a single resolution element to be approximately two photons/sec; obviously, the single-to-noise ratio ( $\approx 10^6$  to  $10^7$ ) is adequate for this study.

An additional intensifier system parameter of interest is the photon gain (g), i.e., the number of photons at the output phosphor per photon at the photocathode. The image intensifier parameters which are appropriate for the device used for this study are

Electron Gain (G) = 500 output electrons/photocathode electron

Photon Conversion Efficiency ( $\bar{E}$ ) = 0.05 output photons/output electron/eV

Effective Accelerating Voltage (V) = 2.5 keV

Photocathode Efficiency ( $\zeta$ ) at 500 nm = 0.10

The photon gain is easily found to be

$$g = \zeta \cdot V \cdot \bar{E} \cdot G$$

or

$$\cong 6 \times 10^3 \text{ output photons/input photon.}$$

---

\*ITT F-4112 intensifier tube

Therefore, assuming an optical system transmission factor of approximately 0.15, one finds the effective photon gain of the intensifier to be on the order of  $10^3$ .

To compare such a system to straight photographic recording, it is easiest to suppose the intensifier output to be recorded by a high-speed cine camera whose framing rate defines the time resolution of the measurement. If such a system is compared with detection by this same cine camera alone, it is obvious that the intensifier system possesses an inherent advantage given by the photon gain, which, in this case, was on the order of  $10^3$ . However, one can obtain a more decisive comparison by considering the minimum detectable signal for photographic recording. A typical minimum energy density for film exposure is on the order of  $0.1 \text{ erg/cm}^2$ . For an area corresponding to that of the minimum resolution element of the intensifier one finds that approximately  $10^6$  photons at 500 nm are required to exceed the typical film inertia. For the particulate-laden flow discussed in a previous paragraph, it was found that the anticipated Mie scattered signal per pixel was on the order of  $10^7$  photons/sec. Therefore, for a 0.1-sec duration flow field, approximately  $10^6$  photons are scattered onto a pixel element area. Consequently, the detectability of such Mie scattering by photographic methods alone is quite marginal for exposure times significantly less than 0.1 sec.

### 3.0 EXPERIMENTAL APPARATUS

On the basis of the results of the feasibility calculation of the previous section the image intensifier system, sketched in Fig. 1, was used to visualize the particle-laden flow field, which was immersed in a nominal Mach 13 flow. The particle injection source was a blunt cone with a base-mounted nozzle of approximately 1-mm diameter. The nozzle centerline was directed outward at 45 deg from the model axis, and the particle exhaust was comprised of nominal  $1\text{-}\mu$ -diam particles borne by helium (He) carrier gas. Further details of the flow field and particle source, although of importance for the analysis of the particle/flow-field interaction, will not be discussed in detail since the purpose of this report is primarily to describe the visualization technique itself. Flow-field properties will be included only when they are essential for evaluating this diagnostic technique.

The experimental geometry utilized in the visualization measurements and sketched in Fig. 1 is shown in more detail in Fig. 3. Source illumination for the particulate plume was supplied by a Coherent Radiation Model CR-3 argon-ion laser operating in the continuous mode at a wavelength of 514.5 nm with a nominal power level of 1.5 watts. The laser (LA) was mounted beneath the tunnel on a vibration isolation table, and it produced a coherent, monochromatic beam of light approximately 2 mm in diameter. This beam was passed through the blades of a chopper (c), which modulated the laser beam at 100 Hz, and was then directed into an optical system by a dielectric mirror.

The optical system consisted of a spatial filter (SF), cylindrical lens (LN), and two limiting apertures which produced a fan-shaped, extended beam approximately 2 mm thick which was directed through the 225-deg port into the wake flow region of the model and passed through a plane formed by the tunnel/model centerline and the axis of the particulate ejection nozzle.

The beam was essentially uniform in intensity across its entire spatial extent and was 19.1 cm (7.55 in.) in width at the tunnel centerline and 20.3 cm (8.0 in.) in width at the particulate ejection orifice (see Fig. 4). The expanding laser beam exited the test section through a quartz window and was intersected by six transmission monitors located at the 45-deg port.

The image intensifier (IT)/fast camera (FC) detection system, shown in Fig. 4, was positioned so that the viewing angle,  $\alpha$ , was 90 deg with respect to the plane of incident laser light. Since only the particles passing through the laser-illuminated region contributed to the scattered light (for the case of visible scattered radiation) the photographic images of the plume viewed in this manner represented a two-dimensional slice through the plume.

The detection system consisted of a collection lens (L1) which gathered the scattered radiation and focused the image of the visualization area onto the active surface of the image intensifier. The intensifier used was an ITT F-4112 with an S-20R spectral response, which is shown in Fig. 5. The electron gain of the tube is nominally 500 for an operating voltage of 5,000 V. The output of the intensifier was focused by a second lens (L2) onto the film of a high-speed, 16-mm Mitchell Monitor Camera. Filters F provide spectral isolation of the scattered radiation. The use of several different filter combinations provided a variety of visualization options. With the incident laser beam unblocked by the chopper and a 514.5-nm narrow bandpass filter, only Mie scattered radiation from the particles was recorded. This filter had a bandwidth of 1 nm full width at half intensity maximum. Utilizing a near-infrared bandpass filter, which transmitted in the region from 700 nm to 1.5  $\mu\text{m}$ , in conjunction with the laser beam blocked by the chopper blades provided for an investigation of the near-infrared particle luminosity. A combination of the data obtained by using both filters provided for transmission in the regions 514.0 to 515.0 nm and 700 nm to 1.5  $\mu\text{m}$  and produced a signal representative of the combination of near-infrared particle luminosity and Mie scattered radiation. With the chopper cycling the laser source radiation from on to off, all of the above visualization cases were obtained.

The intensifier output was recorded using a Mitchell camera which was operated at a rate of 400 frames per second, resulting in a time between frames of 2.5 msec; the frame or photographic time resolution is less than 2.5 msec and is estimated to be approximately 1 msec. Reference times were indicated by comparison with the tunnel arc voltage. Selected

film data frames were digitized utilizing the VKF Image/Analyzer Digitizer System (IADS) and stored on computer disk file for subsequent data processing. (The IADS is a PDP-11-controlled film densitometer device; it measured and stored the data film density as a function of spatial position.) Subsequent data reduction included calibration data for the effects of laser beam intensity profile variations, image intensifier response, and the addition of spatial reference grids. Computer-based data reduction routines were used in analyzing data film frames with respect to light intensity level, and final photographic records were produced with grayness (or color) levels representing scattered intensity levels and lines of constant light intensity. Computer routines also provided for intensity subtraction on a spatial point-by-point basis so that successive frames of near-infrared combined with Mie scattered radiation frames could be combined with alternating pure infrared frames to produce the isolated Mie data.

Six calibrated silicon photodetectors were used to measure the degree of attenuation of the laser radiation as it passed through the particulate plume.

These measurements were made at several spatial locations within the particle plume as indicated in Fig. 6. The laser transmission path to each detector subtended a small volume of the plume, and the attenuation of the laser power along each individual path was recorded as a function of time by the Tunnel F Transient Data System (TDS).

Just prior to each tunnel firing, a laser transmission calibration at tunnel vacuum was recorded on the TDS to provide a maximum transmission (no particle) reference. During the actual run, the TDS recorded the laser transmission channels at 1-msec intervals. Transmission factors were then determined at selected times for further data analysis. Along the laser beam optical path,  $s$ , energy is lost from the incident beam by scattering and absorption. In the absence of multiple scattering, the energy flux of transmitted light is

$$\Phi_{TR} = \Phi_o \exp \left[ - \int_0^S \int_0^\infty \frac{\partial n(x, s)}{\partial x} \sigma_{ext}(x, s) dx ds \right] \quad (5)$$

where  $\sigma_{ext}(x, s)$  is the size parameter ( $x$ )- and position ( $s$ )-dependent extinction cross section and  $S$  is the total path length. Assuming the distribution function to be

$$\frac{\partial n(x, s)}{\partial x} = \bar{n} \delta(x - x_o)$$



where  $\bar{n}$  is the uniform particle density. If the distribution is both monodisperse and spatially uniform, one finds that

$$\Phi_{TR} = \Phi_o \exp \left[ -\bar{n} \sigma_{ext} (x_o) S \right] \quad (6)$$

Therefore, if the size parameter,  $x_o$ , for such a sample is known,  $\sigma_{ext}$  is calculable. Furthermore, the path length (S) can be determined from the visualization photographs, and the transmission ratio  $\tau = \Phi_{TR}/\Phi_o$  can be measured. With these parameters in hand the particle density along the laser beam path is determined.

Additionally, the mass flow rate ( $\dot{m}_p$ ) of the particles can be related to the attenuation of the laser radiation by the particle plume in the following manner:

$$\dot{m}_p = \left( \frac{\pi^2}{24} \right) \rho_s v_p \ell \left( \frac{\bar{D}^3}{\bar{\sigma}_D} \right) \ln (1/\tau) \quad (7)$$

where  $\rho_s$  is the density of the solid particulate,  $v_p$  is the particulate flow speed (flow speed),  $\ell$  is the length of the intersected particulate plume,  $\bar{D}$  is the mean particle diameter,  $\bar{\sigma}_D$  is the mean extinction cross section, and  $\tau$  is the transmission fraction determined as described above. The known optical properties of the particles and the mean particle diameters of the initial samples, determined through independent analysis, were used in conjunction with measured transmission fractions to compute experimentally determined particulate mass flow rates. Transmission path lengths for these computations were determined from the visible visualization photographs. Results could then be compared with mass flow rates determined from model canister weight measurements and mass flow times.

## 4.0 RESULTS

### 4.1 VISUALIZATION RESULTS

Exemplary flow visualization results are presented in Figs. 7 through 13 and summarized in Table 2. Data for several different run conditions and particle compositions are presented to illustrate the wide range of possible visualization data obtainable under the techniques used in this study.

Data from Fig. 7 consisted of Mie scattered radiation combined with near-infrared particulate luminosity. In Fig. 8 pure infrared signal was recorded with the laser source radiation blocked by the chopper blade. Here the particulate plume emanates from the

nozzle, located on the left side of Fig. 8, and expands to the right. Flow direction is from left to right for all data figures. As can be clearly seen, the infrared signal begins somewhat downstream from the nozzle exit and in a region paralleling the bow shock from the model. Indications are that the particles require a short distance or time to interact with the flow before the particle temperature rises sufficiently to produce an infrared signal. Figure 7 was originally recorded with the laser beam on as a combination of visible and near-infrared radiation. In order to obtain a pure visible signal, the pure IR signal V (intensity) from Fig. 8 was subtracted point by point from Fig. 7. One can see from Fig. 7, then, that the visible scattered radiation from the particles clearly traces the particles' exit from the nozzle, their interaction with the bow shock, and their propagation downstream. Obviously, absolute signal levels have been modified in these computer representations for the sake of clarity. The overlying grid lines represent 1-in. squares within the flow and are provided for spatial reference. The particles were pure tungsten (W).

Figure 9 presents typical data from a tungsten carbide particulate plume. Here the data represent almost entirely visible scattered radiation. Again, the particles leave the nozzle in high concentration and expand as they move downstream until they are dispersed to the point that signal levels are below threshold.

Figure 10 illustrates a case of scattering from silicon carbide (SiC) particles. The particulate temperature for this run was very low in comparison with prior runs, and an absence of near-infrared radiation can be discerned.

Figures 11 and 12 graphically illustrate particulate heating upon interaction with the tunnel flow. In Fig. 11, very early in the run, the tungsten carbide (WC) particles display a very weak IR signal and a highly dispersed visible signal. However, much later in the run (Fig. 12), particulate temperature has increased, and a very strong infrared signal is observed. Considerably different run conditions from previous data frames were present, as can be seen from the photographic data summary.

Finally, Fig. 13 illustrates a very hot particulate (1,578K) plume, and a very strong infrared signal is observed.

## 4.2 TRANSMISSION RESULTS

During the course of this measurement program the average particulate mass flow rate ( $\dot{m}_p$ ) was experimentally determined by using the mass loss of the particulate generator and the total ejection time of the particles. It is recalled from Eqs. (6) and (7) that if the particle distribution is uniform in space and monodisperse in size, measurement of the transmission

factor ( $\tau$ ) yields the particle mass flow rate. Even though the Mie scattering photographs vividly show a violation of the assumption of spatial uniformity, it is of interest to apply Eq. (7) and the measured values of  $\tau$  to determine  $\dot{m}_p$ . The results of this exercise are shown in Table 3 for four different tunnel runs. From Table 2 one can see that order-of-magnitude agreement is obtained in all cases with the mass-loss measurement of  $\dot{m}_p$ .

## 5.0 CONCLUSIONS AND RECOMMENDATIONS

The purpose of this report was to demonstrate the capabilities of a Mie scattering-based image intensifier system for particulate diagnostics, and it is suggested that this goal has been achieved. The sensitivity of this system, which employed a high-speed cine camera for recording, obviously exceeds that of the high-speed camera alone, and the capability for qualitative diagnostics of a broad spatial field has been demonstrated. Although it is perhaps obvious, it is significant to note that this diagnostics capability does provide spatial resolution; i.e., scattering occurs only in the region of laser illumination which, in this case, approximates a plane. Further, the time resolution of the system, which was on the order of 1 msec, was limited by the recording camera speed rather than by the sensitivity of the intensifier, which, it should be noted, is a comparatively low gain tube.

Quantitative results of the particulate spatial profiles are obtainable only if certain assumptions are valid. Included in these assumptions are knowledge of the size distribution function, including a monodisperse distribution, and the index of refraction of the particles. Further, use of Eq. (7) to relate the transmission function to the particulate mass flow requires an even more stringent assumption of spatial uniformity of the particles, which Figs. 7 through 13 show would obviously not be valid. Consequently, agreement of particulate mass flux rates as determined by mass loss and transmission techniques to within no better than an order of magnitude is not surprising; in fact, when one acknowledges not only the spatial nonuniformity of the particles but also their known polydispersity, the order-of-magnitude agreement shown in Table 3 is quite gratifying. Quite clearly, for a spatially nonuniform flow field a local measurement of particle speed and number density is required for a local mass flow-rate determination. Such measurements of flow speed have been performed and will be the subject of a future report. Further, for a monodisperse distribution of injected particles the local number density can be determined in a straightforward manner using an in situ calibration. For a polydisperse distribution either particle sizing must be performed or it must be assumed that the size distribution function is spatially invariant; in either event, the local particulate mass flow rate can be determined. In addition, the iso-intensity contours of Figs. 7 through 13 can be reliably and quantitatively interpreted as particulate isodensity contours.

In conclusion, when one incorporates the just-mentioned calibration procedure into the intensifier detection and analysis system, the technique represents a significant enhancement in diagnostic capabilities for study of particle-flow field interactions.

## REFERENCES

1. Born, M. and Wolf, E. *Principles of Optics*. Pergamon Press, New York, 1970 (Fourth Edition).
2. Dave, J. V. "Subroutines for Computing the Parameters of the Electromagnetic Radiation Scattered by a Sphere." Report No. 320 3237, IBM Scientific Center, Palo Alto, California, May 1968.
3. Mundy, W. C., Roux, J. A., and Smith, A. M. "Mie Scattering by Spheres in an Absorbing Medium." *Journal of the Optical Society of America*, Vol. 64, December 1974, pp. 1593-1597.
4. Shaffer, P. T. B. and Naum, R. G. "Refractive Index and Dispersion of Beta Silicon Carbide." *Journal of the Optical Society of America*, Vol. 59, November 1969, p. 1498.

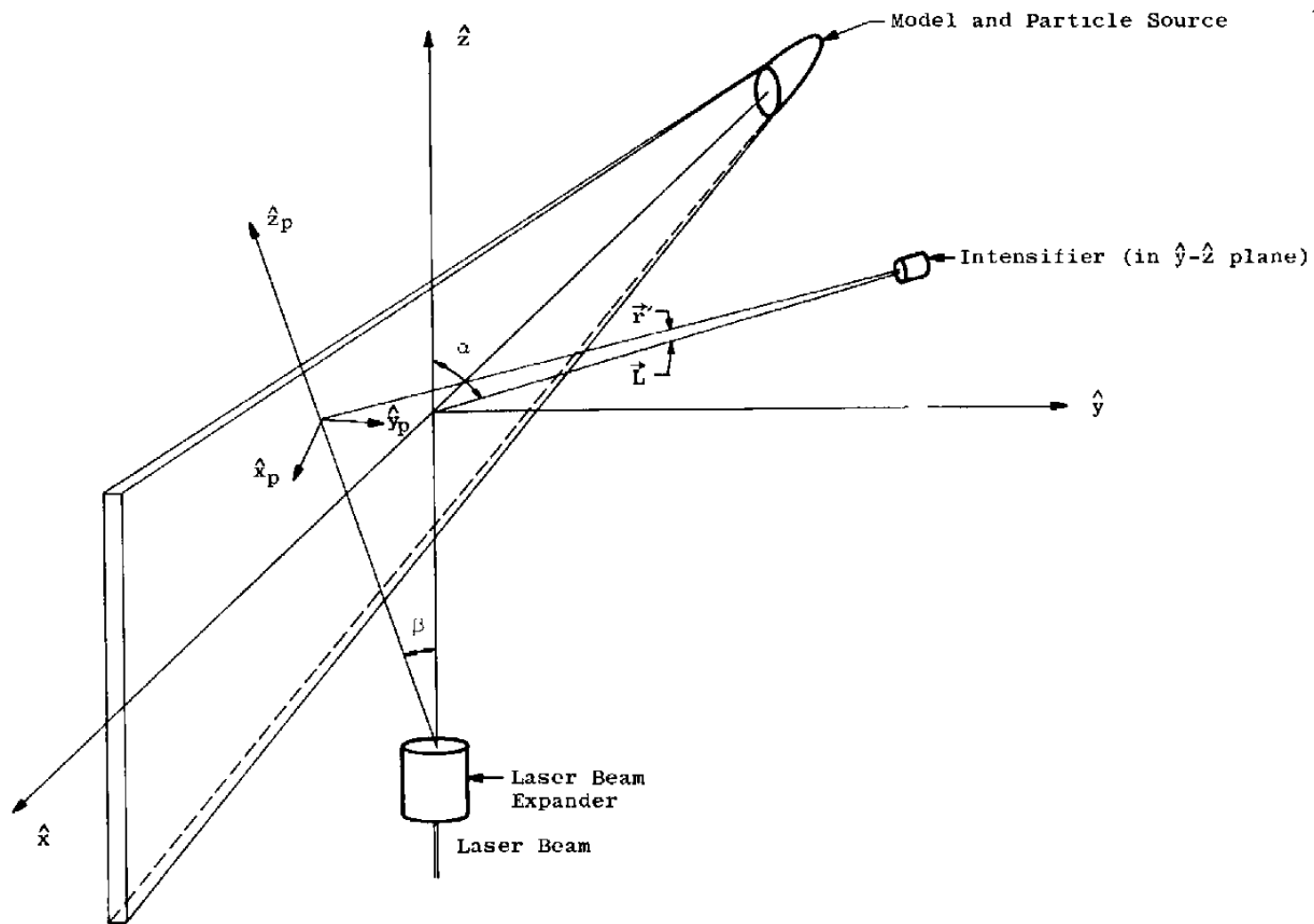


Figure 1. Particle-laden flow-field configuration.

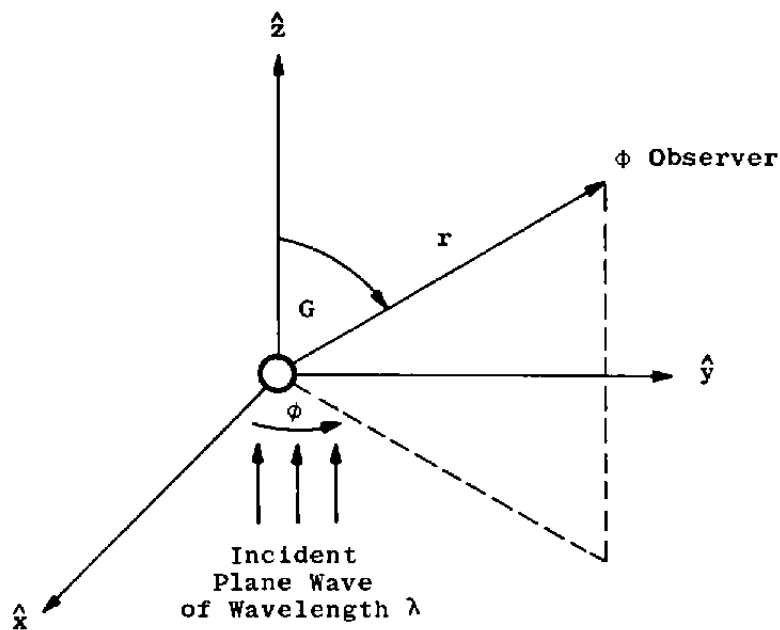


Figure 2. Scattering geometry for single particle with light incident along  $\hat{z}$  axis and polarization vector along  $\hat{x}$  axis.

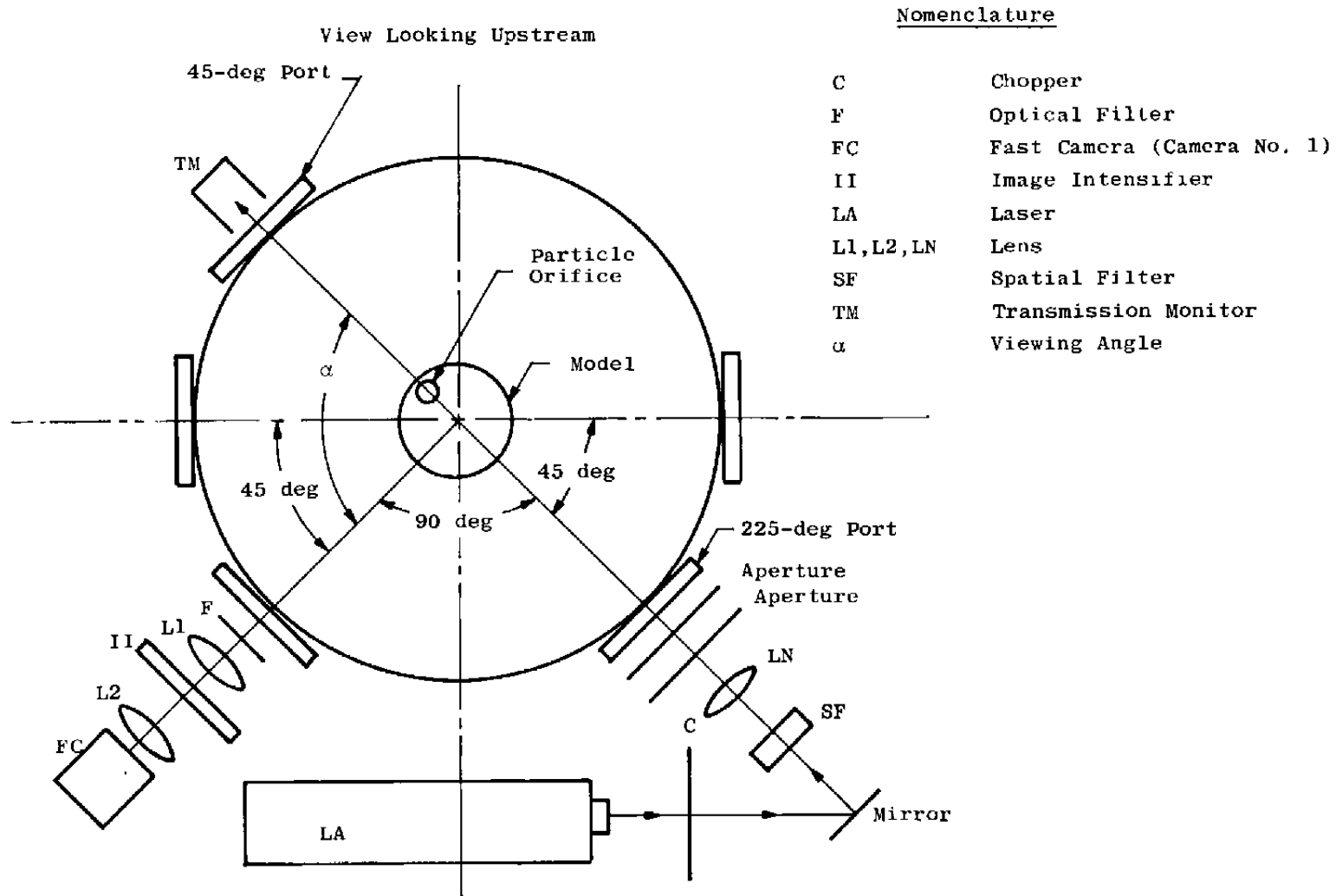


Figure 3. Experimental configuration: Flow visualization and transmission measurements.

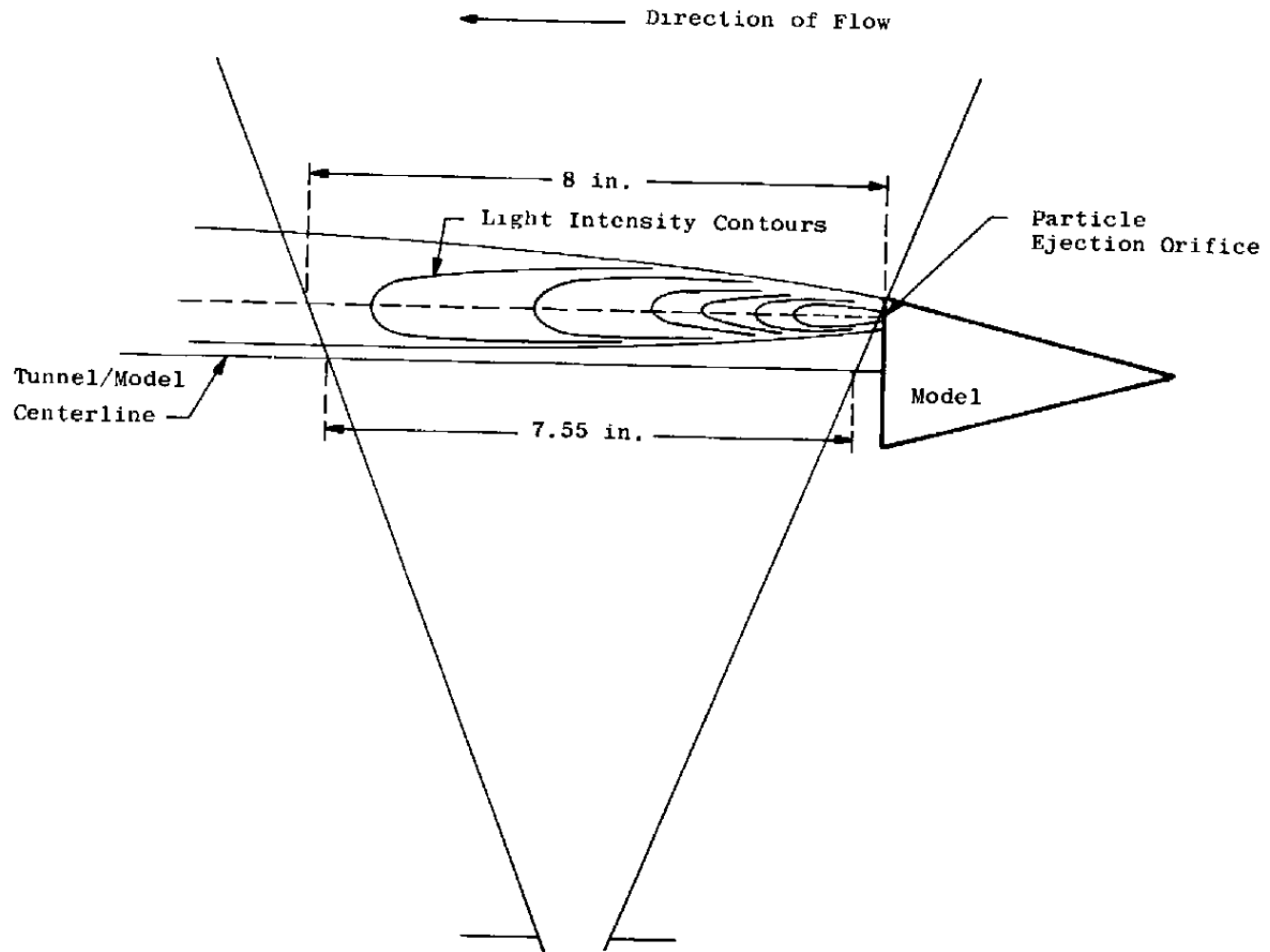


Figure 4. Visualization geometry.



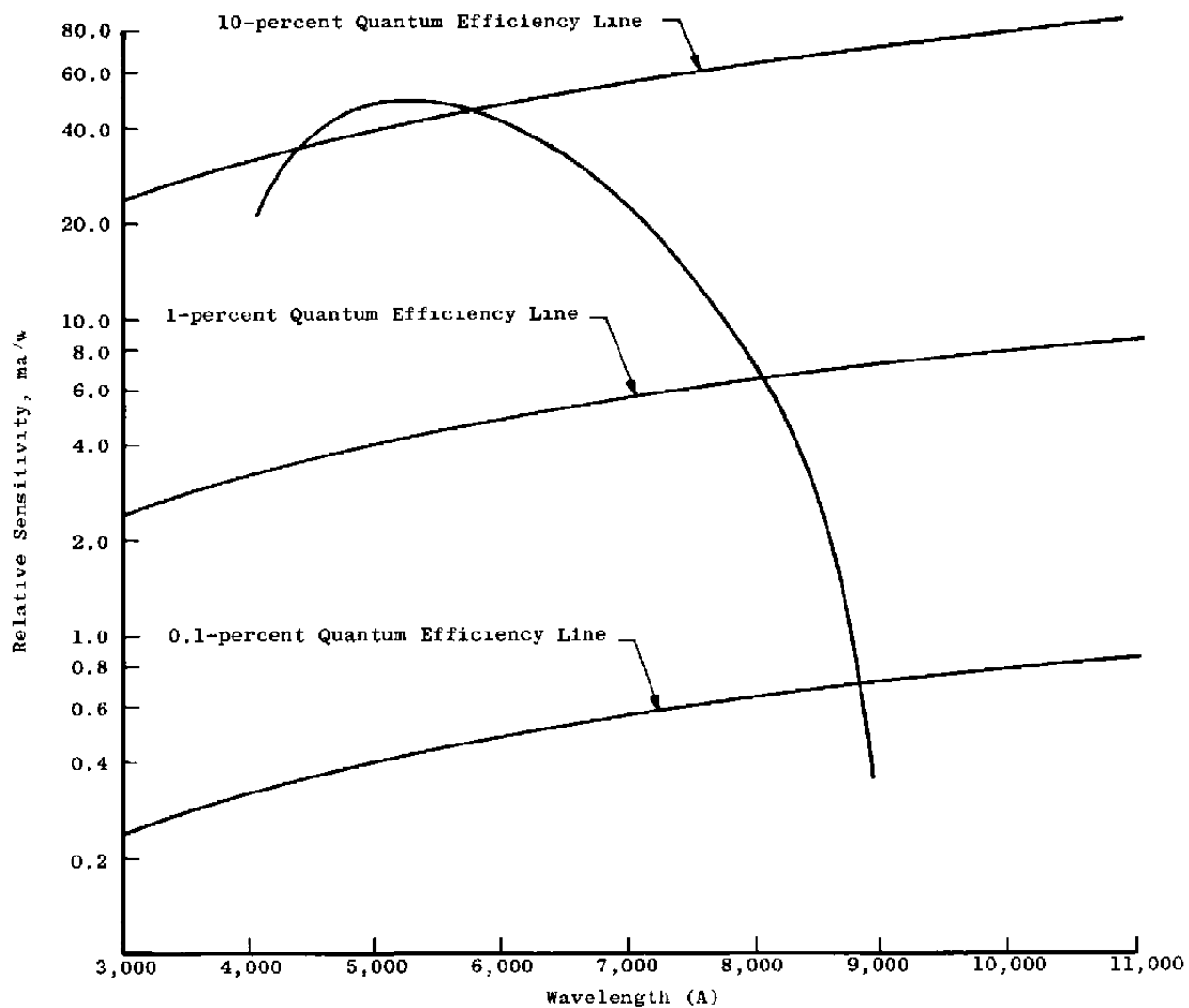


Figure 5. Typical intensifier response curve.

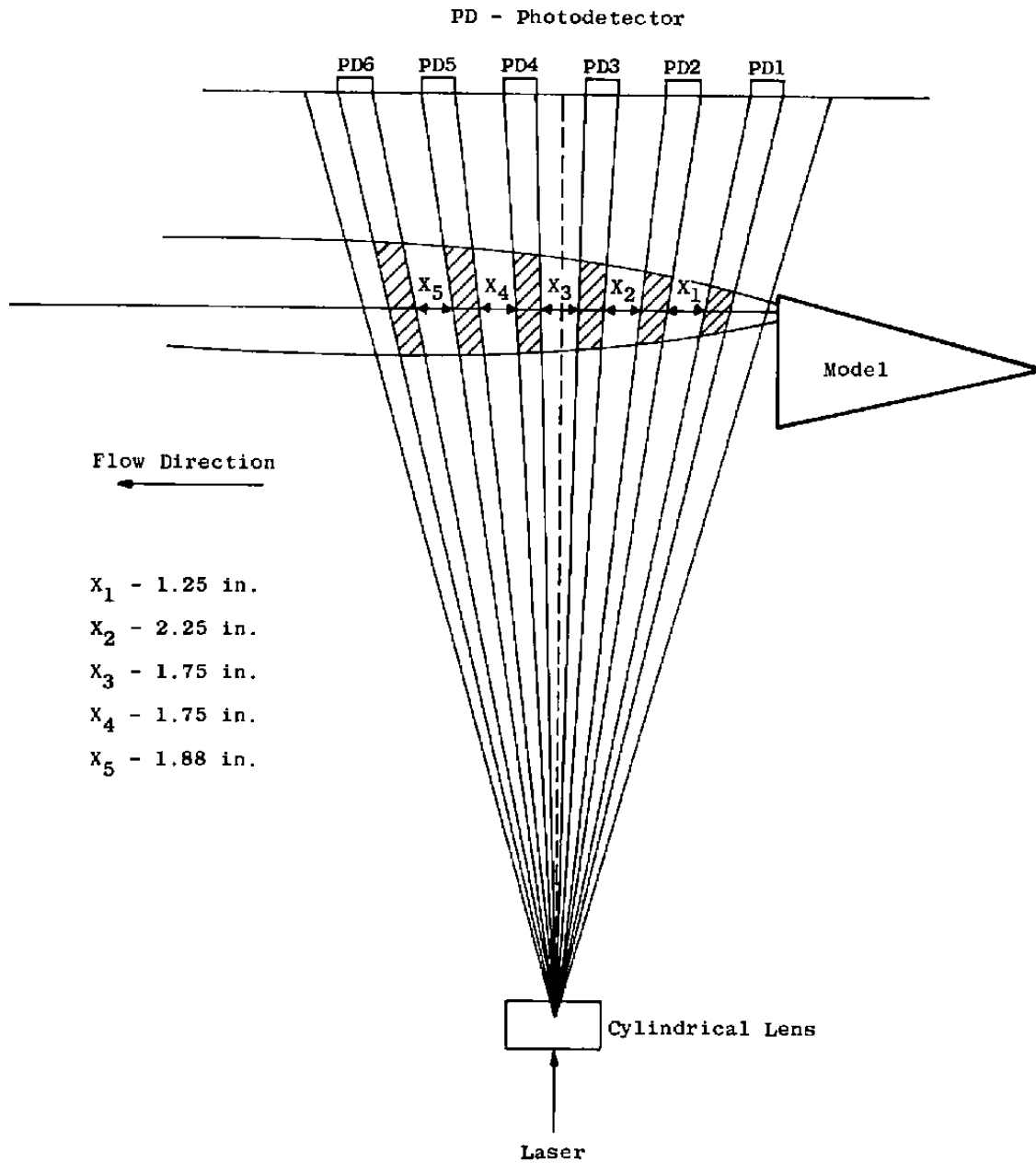
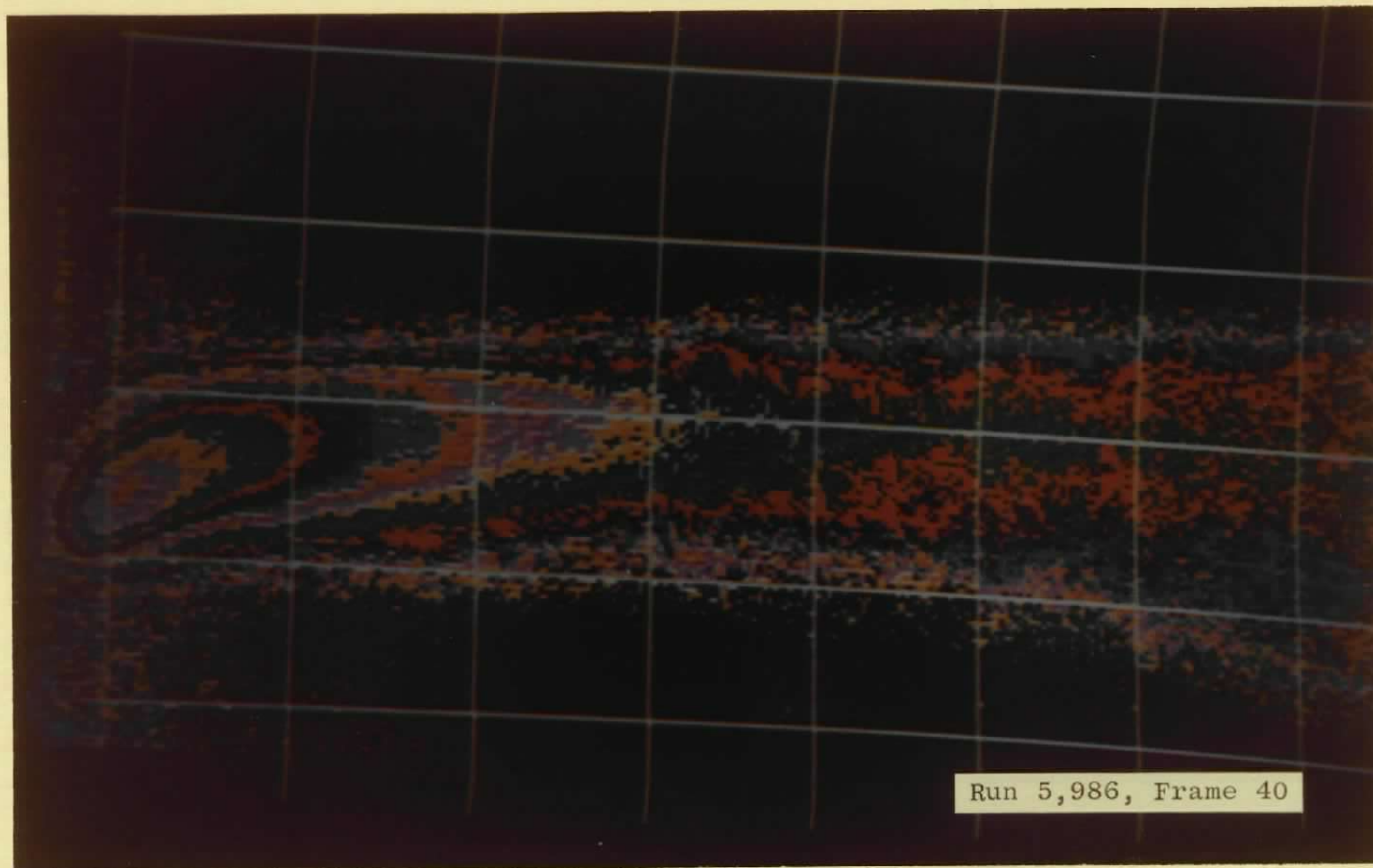


Figure 6. Transmission channel configuration.



**Figure 7.** Flow visualization of tungsten particulate flow, Run 5,986, visualization signal source resulting from Mie scattered radiation combined with near-infrared particulate luminosity.

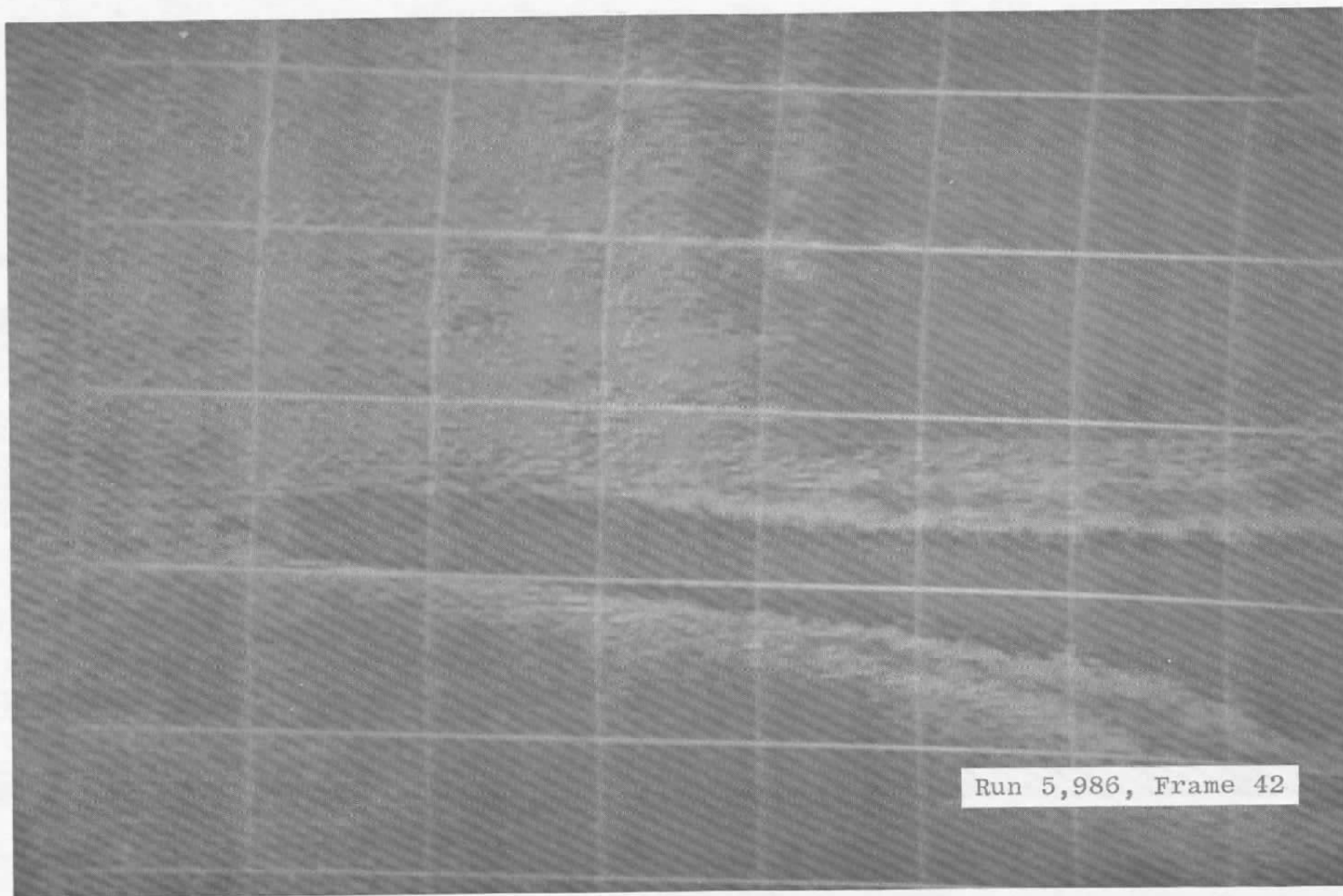


Figure 8. Flow visualization of tungsten particulate flow, Run 5,986, visualization signal source consisting entirely of near-infrared particulate luminosity.

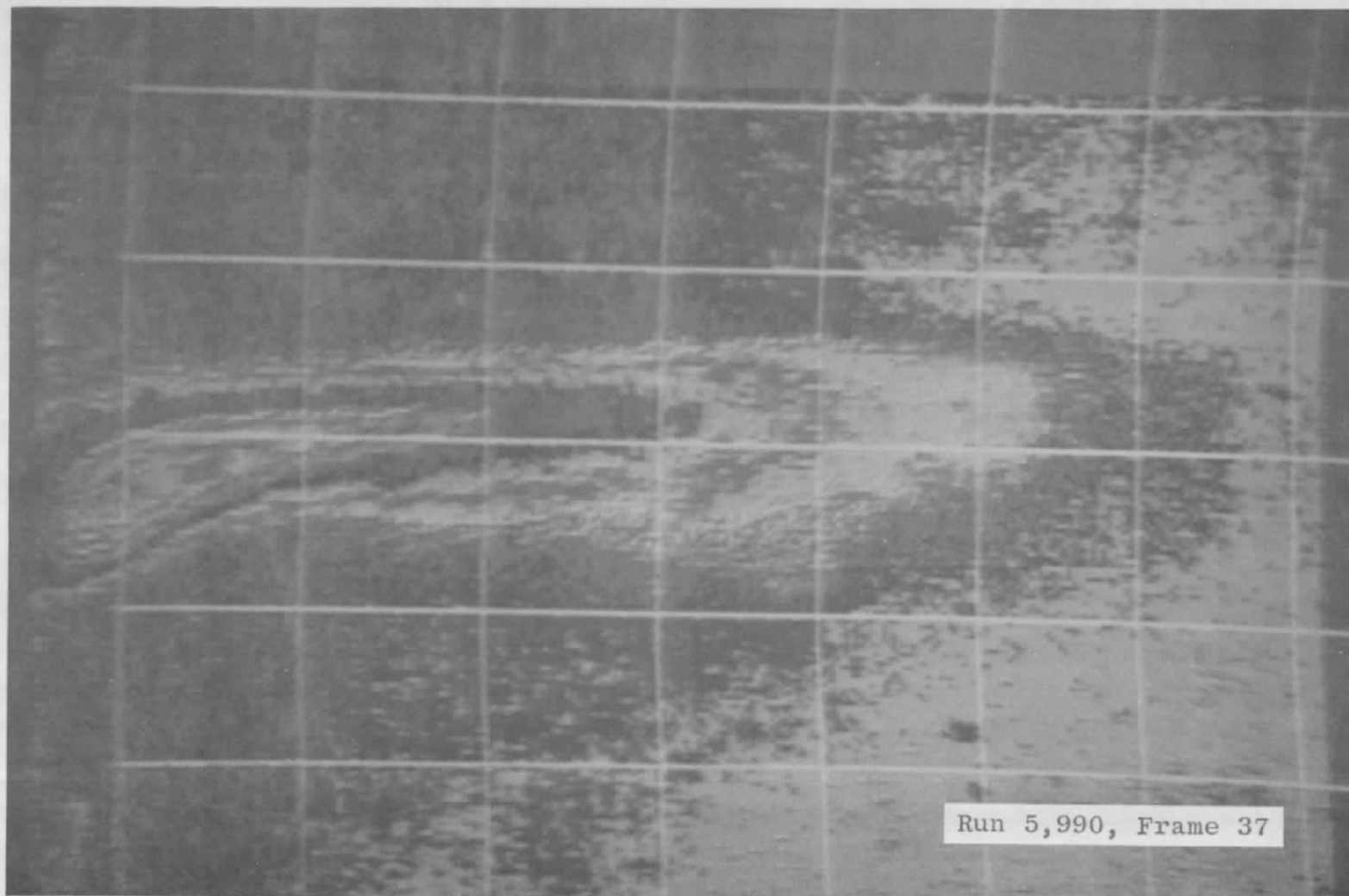


Figure 9. Flow visualization of tungsten carbide particulate flow, Run 5,990, visualization signal source consisting entirely of Mie-scattered radiation.

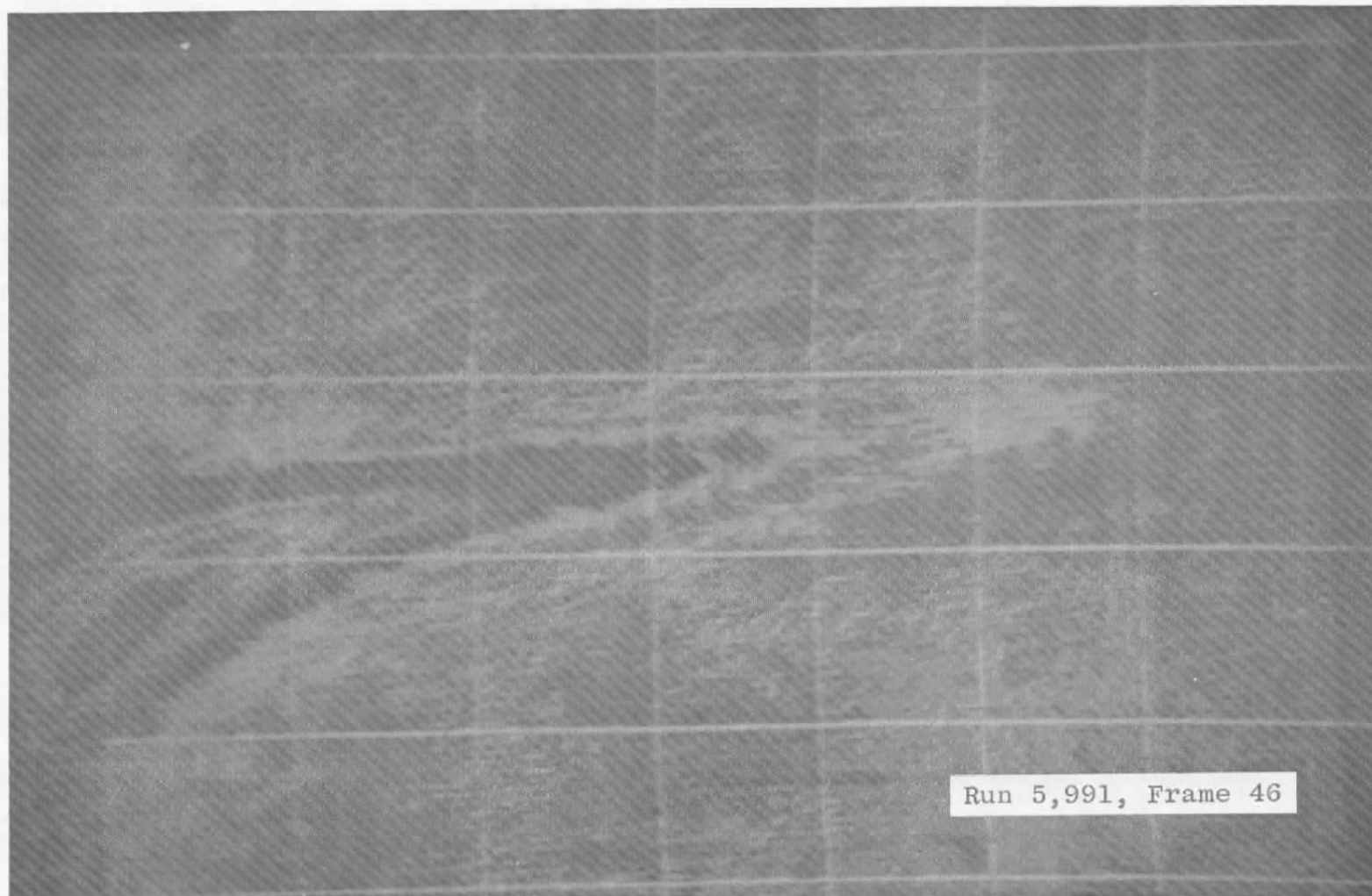


Figure 10. Flow visualization of silicon carbide particulate flow, Run 5,991, visualization signal source resulting from Mie-scattered radiation combined with near-infrared particulate luminosity.

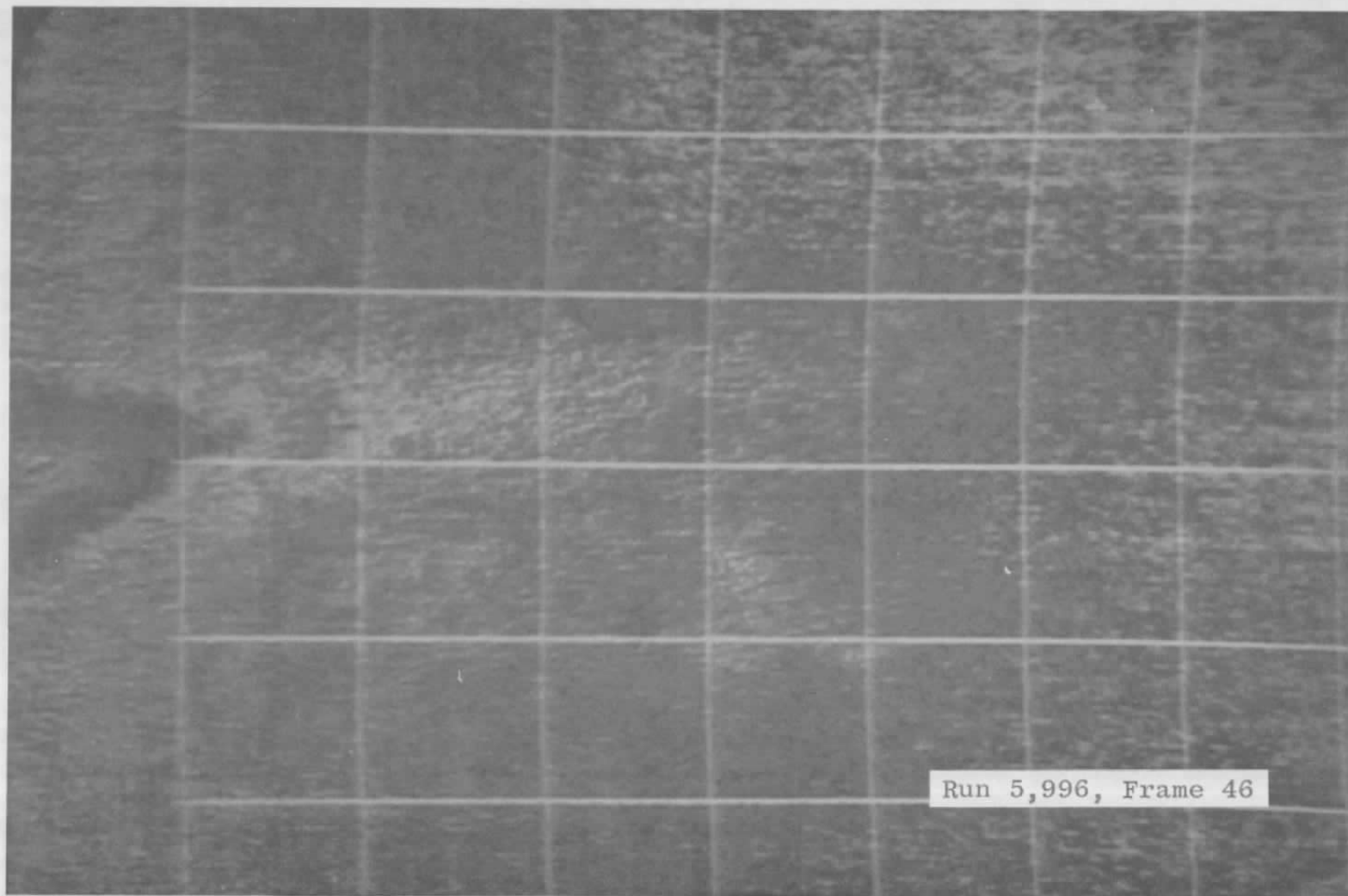
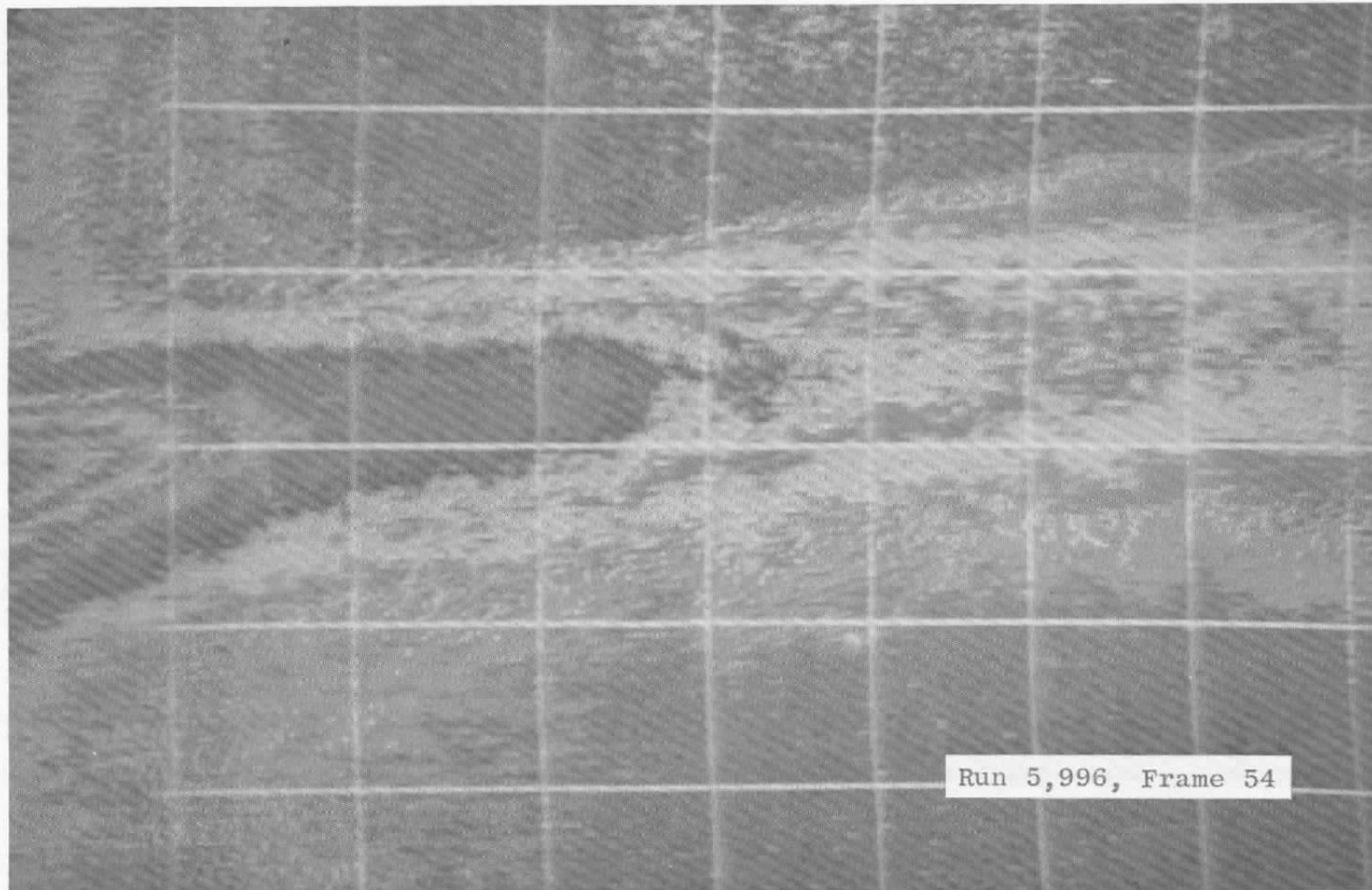


Figure 11. Flow visualization of tungsten carbide particulate flow, Run 5,996 at 111 msec from tunnel arc voltage, visualization signal source consisting of very weak near-infrared particle luminosity and Mie-scattered radiation.





**Figure 12.** Flow visualization of tungsten carbide particulate flow, Run 5,996 at 131 msec from arc voltage, visualization signal source consisting of strong near-infrared particulate luminosity and Mie-scattered radiation.



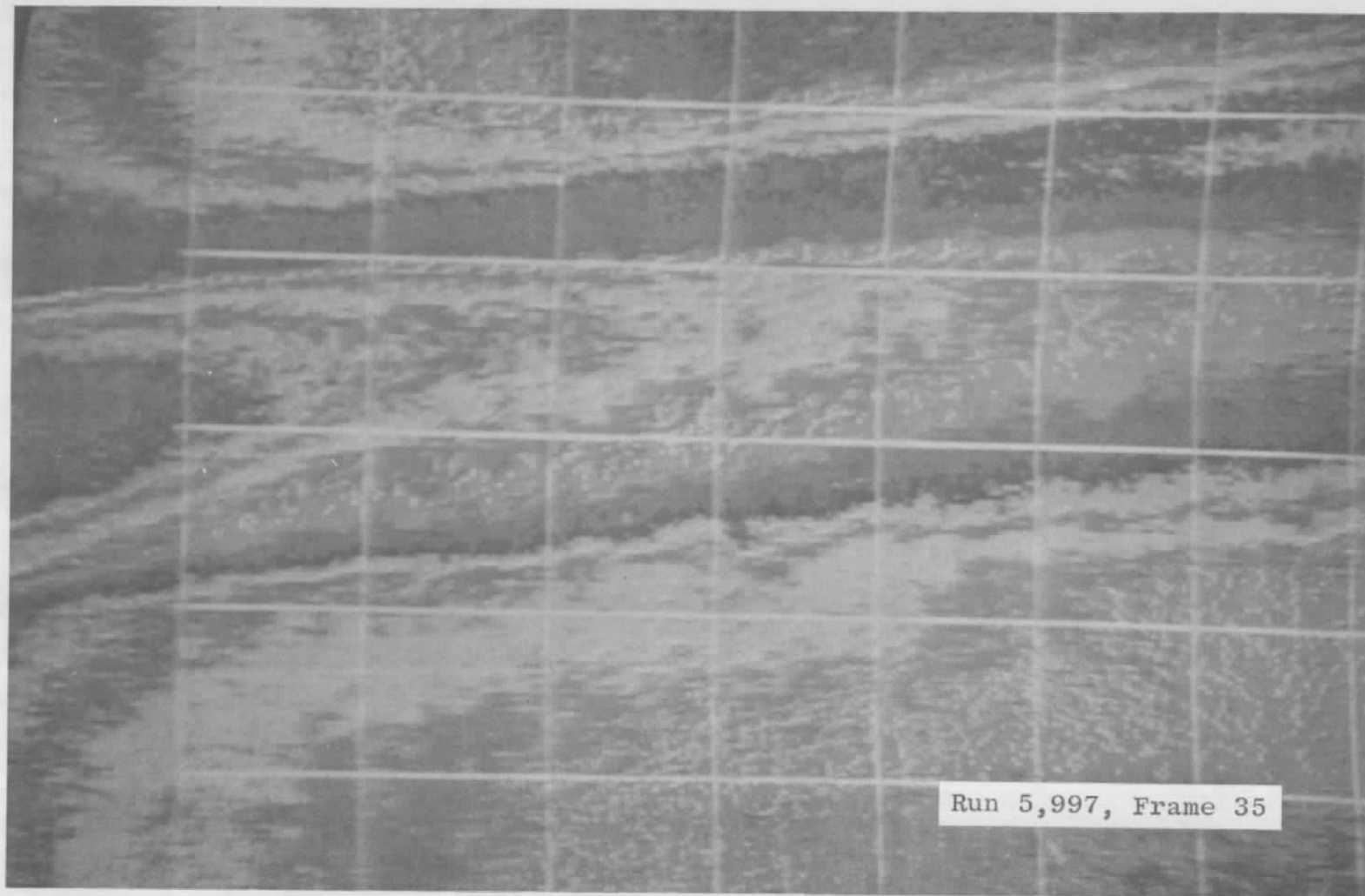


Figure 13. Flow visualization of tungsten particulate flow, Run 5,997, with a particle plume temperature of approximately 1,578 K, visualization signal source consisting of near-infrared particulate luminosity and Mie-scattered radiation.

Table 1. Flux Integral IF

x	$\alpha = 45 \text{ deg}$	$\alpha = 90 \text{ deg}$
5.11	31.9	7.9
6.11	57.6	2.3
7.11	146.9	3.8
8.11	38.4	26.4

Table 2. Exemplary Data Photograph Summary

Number	Particle	Time from Arc Voltage, msec	$Re_{\omega} \times$ $10^{-6}/ft$	$T_o$ , K	Equivalent Blackbody Plume Temp., K	Radiation Source
7	W	96	2.88	2,042	1,302	Visible (514.5 nm)
8	W	101	---	---	---	Near-IR (700 nm-1.5 $\mu$ m)
9	WC	89	2.25	2,210	1,138	Near-IR (700 nm-1.5 $\mu$ m)
10	SiC	111	2.74	1,964	-Low-	Visible + (Weak) IR
11	WC	111	0.8	2,232	1,113	Visible + (Very Weak) IR
12	WC	131	---	---	---	(Strong) IR + Visible
13	W	84	0.47	2,868	1,578	(Very Strong) IR + Visible

Table 3. Mass Flow Rate — Exemplary Data Summary

Run	Particle	$\dot{m}_p$ (Transmission), gm/sec	$\dot{m}_p$ (Weight), gm/sec
1	SiC	4.22	1.0
2	W	3.50	4.4
3	SiC	1.91	1.33
4	W	3.91	4.3

Table 4. Exemplary Transmission Data

Figure Number	Time from Arc Voltage, msec	Chopper	Particle Material	Particle Concentration (Particles/cm <sup>3</sup> )					
				PD1	PD2	PD3	PD4	PD5	PD6
7	124	Yes	W	---	$2.63 \times 10^6$	---	---	---	---
8	116	Yes	WC	$1.51 \times 10^5$	$1.48 \times 10^5$	$1.31 \times 10^5$	$6.88 \times 10^4$	$6.11 \times 10^4$	$5.27 \times 10^4$
9	111	Yes	SiC	$2.76 \times 10^5$	$2.37 \times 10^5$	---	$1.18 \times 10^5$	$5.98 \times 10^4$	$2.15 \times 10^4$
10	111	No	W	$5.07 \times 10^5$	$8.16 \times 10^5$	$4.31 \times 10^5$	$2.44 \times 10^5$	$3.36 \times 10^5$	$3.04 \times 10^5$
11	120	No	SiC	$2.97 \times 10^5$	$2.69 \times 10^5$	$1.07 \times 10^5$	$4.28 \times 10^4$	$3.11 \times 10^4$	$5.97 \times 10^4$
12	125	No	WC	$6.22 \times 10^4$	$9.89 \times 10^4$	$7.35 \times 10^4$	$5.91 \times 10^4$	$5.27 \times 10^4$	$2.43 \times 10^4$
13	119	No	W	$1.44 \times 10^5$	$2.57 \times 10^5$	$2.86 \times 10^5$	$1.50 \times 10^5$	$1.03 \times 10^5$	$6.91 \times 10^4$

PD - Photodetector

## NOMENCLATURE

$A_{\text{beam}}$	Area of source beam
$A_o$	Area of pixel
$\bar{D}$	Mean particle diameter
$d$	Thickness of incident laser sheet
$\bar{E}$	Photon conversion efficiency
$F$	Optical filters within the collection optics path
$FC$	Fast camera
$f, L1, L2$	Focal lengths of lenses within the image intensifier optical path
$G$	Electron gain
$g$	Image intensifier photon gain
$I$	Intensity of scattered radiation
$I_o$	Incident laser intensity
$IF$	Flux integral
$II$	Image intensifier
$i_{1,2}$	Mie intensity functions
$k$	Wave number of incident light
$L$	Distance from flow centerline to image intensifier
$LN$	Cylindrical lens
$\ell$	Position of scattering center along laser path (Section 2); length of intersected particulate plume (Section 3)
$M$	Demagnification factor
$\dot{m}_p$	Mass flow rate of particles
$n$	Particle number density
$\bar{n}$	Particle number density averaged over path length, $s$

$R_b$	Radius of plume boundary
$r$	Distance from scattering event to detector
$r, \theta, \phi$	Polar coordinates (axis shown in Fig. 2)
$S$	Total path length of laser beam
SF	Spatial filter
$s$	Laser beam optical path along which scattering and absorption occur
$V$	Effective accelerating voltage
$v_p$	Particulate flow velocity
$X$	Particle size parameter
$\hat{x}, \hat{y}, \hat{z}$	Rectangular coordinate system as shown in Fig. 1
$x_0$	Half the axial "look distance"
$Z_L$	Distance from flow centerline to laser source
$\alpha$	Angle separating directions of laser propagation and intensifier optical axis (Section 2)
$\beta$	Angle of divergence of injection beam
$\beta_0$	Beam divergence angle with $-\beta_0 \leq \beta \leq \beta_0$
$\zeta$	Photocathode efficiency
$\eta$	Index of refraction relative to the medium
$\eta_r$	Real part of index of refraction
$\theta$	Polar scattering angle (Section 2)
$\kappa$	Imaginary part of index of refraction
$\lambda$	Wavelength of incident light in the scattering medium
$\rho_s$	Density of solid particulate
$\sigma$	Scattering cross section integrated over solid angle subtended by detector
$\sigma_{\text{ext}}$	Extinction cross section

$\bar{\sigma}_0$	Mean extinction cross section
$\tau$	Transmission ratio
$\Phi$	Scattered power
$\Phi_0$	Incident laser power
$\phi$	Azimuth of the scattering plane

## SUBSCRIPTS

o	Incident
1	Denotes scattering state with electric vector perpendicular to scattering plane
2	Denotes scattering state with electric vector parallel to scattering plane
s	Denotes parameters specific to scattering volume and angles
TR	Denotes transmitted beam